Trends in electrocatalysis on extended and nanoscale Pt-bimetallic alloy surfaces

VOJISLAV R. STAMENKOVIC[1,2]*, BONGJIN SIMON MUN[2,3], MATTHIAS ARENZ[4], KARL J. J. MAYRHOFER[5], CHRISTOPHER A. LUCAS[5], GUOFENG WANG[6], PHILIP N. ROSS[2] AND NENAD M. MARKOVIC[1]*

[1]Materials Science Division, Argonne National Laboratory, Argonne, Illinois 60439, USA
[2]Materials Sciences Division, Lawrence Berkeley National Laboratory, University of California, Berkeley, California 94720, USA
[3]Department of Applied Physics, Hanyang University, Ansan, Kyunggi-Do 426-791, Korea
[4]Technical University of Munich, 80333 Munich, Germany
[5]Oliver Lodge Laboratory, Department of Physics, University of Liverpool, Liverpool L69 7ZE, UK
[6]Department of Chemistry and Physics, University of South Carolina, Aiken, South Carolina 29801, USA
*e-mail: vrstamenkovic@anl.gov; nmmarkovic@anl.gov

Published online: 18 February 2007; doi:10.1038/nmat1840

One of the key objectives in fuel-cell technology is to improve and reduce Pt loading as the oxygen-reduction catalyst. Here, we show a fundamental relationship in electrocatalytic trends on Pt_3M (M = Ni, Co, Fe, Ti, V) surfaces between the experimentally determined surface electronic structure (the *d*-band centre) and activity for the oxygen-reduction reaction. This relationship exhibits 'volcano-type' behaviour, where the maximum catalytic activity is governed by a balance between adsorption energies of reactive intermediates and surface coverage by spectator (blocking) species. The electrocatalytic trends established for extended surfaces are used to explain the activity pattern of Pt_3M nanocatalysts as well as to provide a fundamental basis for the catalytic enhancement of cathode catalysts. By combining simulations with experiments in the quest for surfaces with desired activity, an advanced concept in nanoscale catalyst engineering has been developed.

The development of new materials that can solve challenging problems in the areas of clean energy production, conversion and storage is of paramount importance in the quest to find an alternative to environmentally unfriendly fossil-fuel use. One promising alternative is the polymer electrolyte membrane fuel cell[1–6], a device in which hydrogen, through its reaction with oxygen, produces water as its only product. To make hydrogen-based energy systems a vibrant and competitive force, many problems still need to be solved[7]; the main one being to find a more effective catalyst than Pt for the oxygen-reduction reaction (ORR), the cathodic half-cell reaction in the hydrogen–oxygen (air) fuel cell ($1/2O_2 + 2H^+ + 2e^- = H_2O$).

Electrocatalysts with unique properties can be created by alloying two or more metals. Several investigations[8–11] have been carried out to determine the role of alloying in the electrocatalytic activity of Pt for the ORR; a definitive determination, however, remains elusive. For example, a series of binary PtM alloys (M = Cr, Mn, Co, Ni) supported on carbon produced some enhancement in the kinetics of the ORR (a factor of 3–5, ref. 12) relative to 'standard' supported Pt catalysts. One of the difficulties in determining the effect of alloying using supported catalysts, however, is that the activity of a supported catalyst can have a wide range of values depending on its microstructure and/or method of preparation. The intrinsic activity of nanoparticles depends on particle size, shape and composition[9,13], that is, there is no single value of the specific activity even when normalized by Pt surface area. As the alloyed Pt-catalyst particles may not have either the same particle size or shape as the Pt catalysts with which they are compared, a simple comparison of activity normalized either by mass or surface area is insufficient to identify a true alloying effect. Furthermore, because both the surface segregation and segregation-induced changes in the surface electronic properties are unknown for Pt-bimetallic nanoparticles, the effect of chemical composition and/or atomic/electronic surface structure on reactivity is still unresolved. These complexities regarding supported catalysts emphasize the need for using well-characterized materials to identify the fundamental mechanisms at work in the ORR.

Here, emphasis is placed on advanced concepts that can be used to understand and predict variations in the ORR reactivity caused by the effects of alloying Pt with the 3*d*-transition metals. Electrocatalytic trends in the ORR are established as a relation between the surface composition, specific activity (kinetic current density, $\mathbf{i_k}$) and the surface electronic structure of Pt_3M (M = Ni, Co, Fe, V, Ti) alloy surfaces.

Before exploring trends in catalytic activity, it is important to describe, briefly, the ultrahigh-vacuum (UHV) methodology used to prepare (sputtering/annealing cycles) and to characterize the cleanliness (Auger electron spectroscopy, AES), the composition of the surface atomic layer (low-energy ion scattering, LEIS) and the electronic surface structure (ultraviolet photoemission spectroscopy, UPS) of the Pt_3M alloy surfaces. As the preparation/characterization methodology is the same for all Pt_3M alloys[14,15], the results for Pt_3Fe are described as a representative case. AES spectra of Pt_3Fe, shown in Fig. 1a, reveal that after sputtering/annealing cycles, the surfaces are free of impurities such as C and O. The Pt/Fe AES peak ratio is reduced on a sputtered surface compared with an annealed surface. This was the first

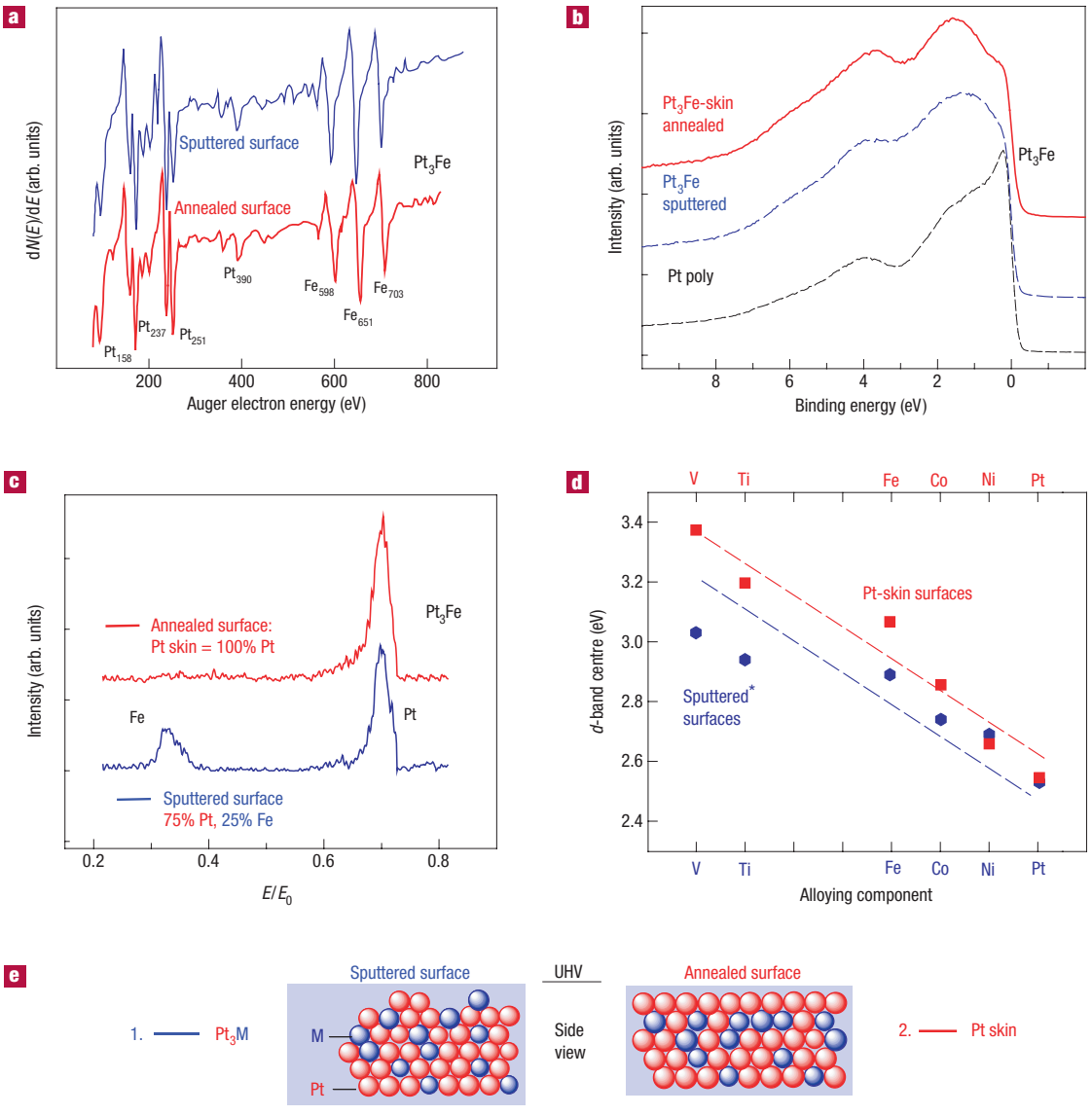

Figure 1 UHV surface characterization of a Pt_3Fe alloy. a–c, AES, 3 keV (**a**), UPS, 90 eV (**b**) and LEIS, Ne^+ 1 keV (**c**) spectra of mildly sputtered and annealed surfaces. **d**, The *d*-band centre position obtained from the valence-band spectra of Pt_3M alloy surfaces (sputtered surfaces*) and Pt-skin surfaces relative to the Fermi level. **e**, Schematic model for Pt_3M (1) and Pt-skin surfaces (2).

indication that the concentration profile of the Pt and Fe atoms in the near-surface region is dependent on the pretreatment of the Pt_3Fe surface. The exact composition of the topmost atomic layer of Pt_3Fe was obtained from analysis of the LEIS spectra. Figure 1c shows that, whereas after mild sputtering the composition of the first outermost layer is the same as that in a bulk Pt_3Fe alloy (that is, 75% of Pt and 25% of Fe), after annealing the surface atomic layer was pure Pt owing to the surface segregation. Both experimental and theoretical studies have shown that Pt surface enrichment in Pt_3M systems is counterbalanced by the depletion of Pt in the next two to three atomic layers, resulting in a concentration profile that oscillates around the bulk value[16,17]. To make a distinction between bulk-terminated and segregated Pt-rich surfaces (see Fig. 1e), the latter have been termed 'Pt skin'. As shown below, these surfaces have unique surface, electronic and catalytic properties.

To characterize the surface electronic properties of Pt_3Fe, synchrotron-based high-resolution UPS was used[18]. The background-corrected UPS spectra of the Pt_3Fe surfaces, see Fig. 1d, show that the electronic structure of an annealed surface is different from that obtained after sputtering (bulk-terminated surface composition). In particular, the density of state (DOS) near the Fermi level is reduced after the annealing process, that is, the position of the *d*-band centre shifts from −2.89 eV on the sputtered surface to −3.05 eV on the annealed surface (bulk Pt has a value of −2.54 eV). Given that the same tendency is found for other Pt_3M alloys, we conclude that, irrespective of the particular 3*d* element, the *d*-band centre of annealed surfaces is always downshifted relative to that of sputtered surfaces. The relation between the position of the *d*-band centre and the nature of the 3*d* element, shown in Fig. 1d, is linear, which agrees well with theoretically predicted variations in the surface *d*-band centre of Pt(111) slabs containing subsurface 3*d* metals, the so-called 'sandwich' structures[19,20]. Although the polycrystalline alloys are more complex than model structures, in this work, the

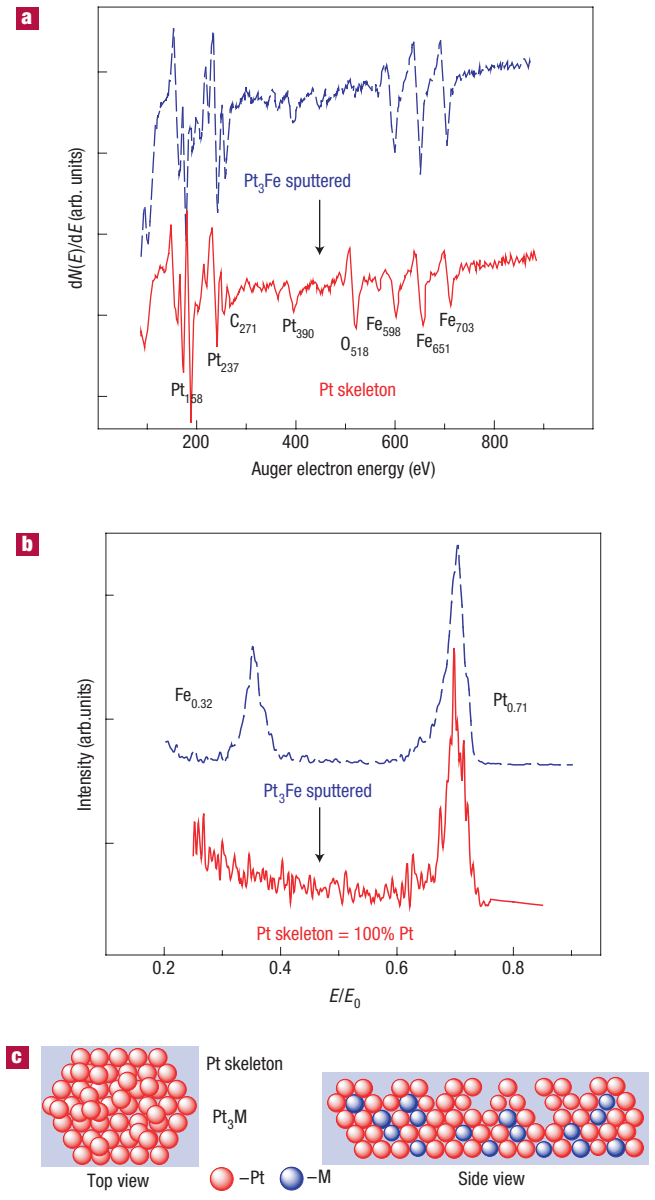

Figure 2 Stability of Pt_3Fe in the electrochemical environment. a,**b**, AES, 3 keV (**a**) and LEIS, Ne^+ 1 keV (**b**) spectra of a mildly sputtered Pt_3Fe alloy before (blue curves) and after (red curves) exposure to an electrochemical environment. **b**, A schematic model for the Pt-skeleton layer to help visualize the structure and composition of Pt and M atoms in the near-surface region.

experimentally determined *d*-band centres are used to establish the electrocatalytic trends for the ORR on different alloy surfaces.

Before discussing electrocatalytic trends, it is important to explore the stability of UHV-prepared surfaces in the electrochemical environment, a subject that is seldom addressed yet is crucial in engineering catalysts for practical applications. For this purpose, an *ex situ* approach was adopted, that is, sputtered and annealed surfaces were transferred from UHV into an electrochemical cell and cycled in the potential region relevant to ORR ($0.05\,V < E < 1.0\,V$). Following electrochemical experiments, the surfaces were rinsed with water and then returned into UHV for post-electrochemical examination. As shown in Fig. 2, the AES/LEIS spectra recorded on the sputtered surface before and after emersion are very different. In particular, whereas Fig. 2a shows that after emersion of the Pt_3Fe electrode from 0.1 M $HClO_4$ the AES signals for Fe are attenuated, Fig. 2b reveals that only the Pt peak is observed in the LEIS spectra. Therefore, on the basis of the AES/LEIS results, it seems that Fe dissolves from the surface when in contact with electrolyte, so that the remaining surface layer is pure Pt. However, the composition of the subsurface layers is unchanged, that is, it is bulk-terminated, as shown in the schematic model in Fig. 2c. The conclusions reached for the Pt_3Fe surfaces are also valid for the other Pt_3M alloys. In contrast, the AES/LEIS spectra obtained from the annealed Pt_3M surfaces before and after emersions were the same, implying that the Pt skin formed in UHV is rather stable in the electrochemical environment and that the Pt-skin surface acts as a protective layer for the atomic layers underneath. To distinguish between the Pt-skin surface and the Pt surface layer formed after dissolution of the 3*d* element, the latter is designated as the 'Pt-skeleton' surface. The schematic models shown in Figs 1e and 2c summarize two important differences between the Pt-skeleton and Pt-skin layers: (1) the morphology of the Pt surface atoms is different, that is, the Pt-skeleton surface is more corrugated; and (2) in contrast to an oscillating concentration profile, proposed for the Pt-skin surface, in the case of the Pt-skeleton surface, a bulk-like alloy concentration profile is present up to the subsurface atomic layer.

Further surface characterization was done by cyclic voltammetry after clean transfer from UHV to the electrochemical environment. By integrating the charge under the voltammogram of the Pt-skin and Pt-skeleton surfaces, the fractional surface coverages for the adsorption of underpotentially deposited hydrogen[6] and hydroxyl species ($2H_2O = OH_{ad} + H_3O^+ + e^-$) were estimated. Careful inspection of the cyclic voltammograms in Fig. 3a reveals that on the Pt-skin surface there is a clearly discernible positive shift in OH_{ad} formation ($E > 0.7\,V$) relative to pure Pt, whereas the onset of OH_{ad} adsorption on the Pt-skeleton surface falls in between the two. In agreement with the onset of OH_{ad} adsorption, the oxide reduction peak obtained in the cathodic sweep for the Pt-skeleton surface lies between the one for pure Pt and the Pt skin, confirming that the OH_{ad} chemisorption energy increases as the *d*-band centre moves closer to the Fermi level[20], that is, the decrease in fractional coverage by OH_{ad} follows the same trend: Θ_{OH}-skin $< \Theta_{OH}$-skeleton $< \Theta_{OH}$-Pt. Moreover, the same trends are also observed for the underpotentially deposited hydrogen adlayer, suggesting that, as predicted by theory for metal–gas interfaces[19,21–24], at electrified metal–solution interfaces, the *d*-band centre can be used as a measure of the strength of the metal–adsorbate interaction[15,20]. As the Pt skin and thus its segregation profile remain stable during the ORR (Fig. 3b), the electronic properties of the Pt-skin surfaces at the metal–electrolyte interface should be considered to be the same as those established in UHV (which is not the case for Pt-skeleton surfaces). Therefore, the discussion of electrocatalytic trends for the ORR will be primarily focused on the Pt-skin surfaces.

The ORR is a multielectron reaction that may include a number of elementary steps involving different reaction intermediates. Recent studies[25–28] have suggested that a series pathway via an $(H_2O_2)_{ad}$ intermediate may be operative on Pt and Pt-bimetallic catalysts and the rate-determining step is the first electron transfer to $O_{2,ad}$. The rate expression is then[27,29,30],

$$i = nFKc_{O_2}(1-\Theta_{ad})^x \exp(-\beta FE/RT)\exp(-\gamma \Delta G_{ad}/RT), \quad (1)$$

where $n, F, K, c_{O_2}, R, x, \beta$ and γ are constants[27], E is the electrode potential, T is the temperature and Θ_{ad} is the total surface coverage by spectator species, for example, OH_{ad} ($\Theta_{OH_{ad}}$), specifically adsorbed anions (Θ_{Aad}) and ΔG_{ad} is the Gibbs energy of adsorption

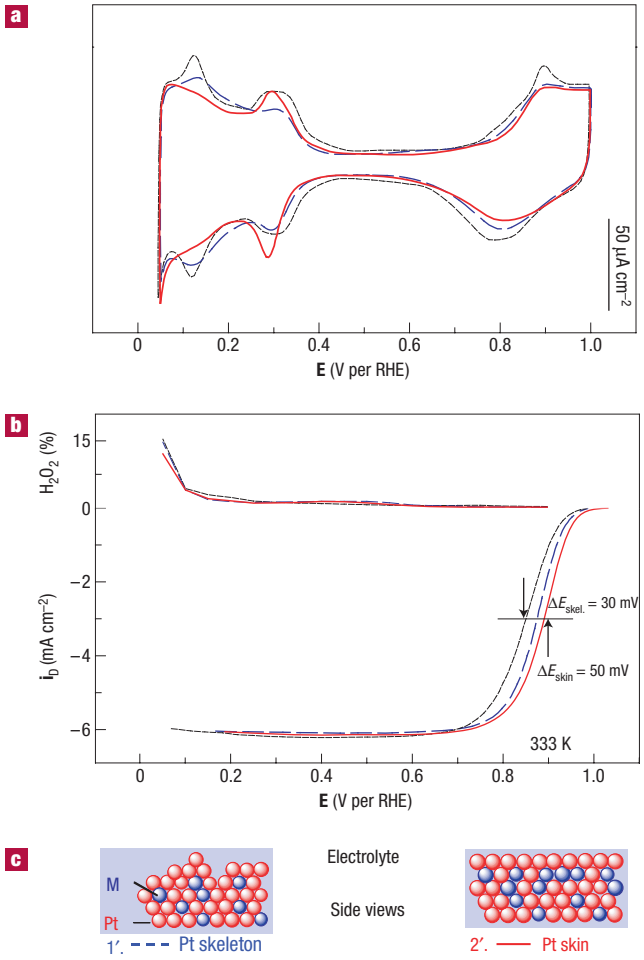

Figure 3 Electrochemical properties of Pt_3Fe surfaces. a, Cyclic voltammograms of the Pt-skeleton (blue line) and Pt-skin (red line) electrodes as well as for a pure polycrystalline Pt (black line) electrode in 0.1 M $HClO_4$. **b**, Polarization curves for the ORR on the disc electrode and the corresponding fraction of peroxide detected on the ring electrode. **c**, Schematic models showing that Pt skin and Pt skeleton are stable surface formations in the electrochemical environment.

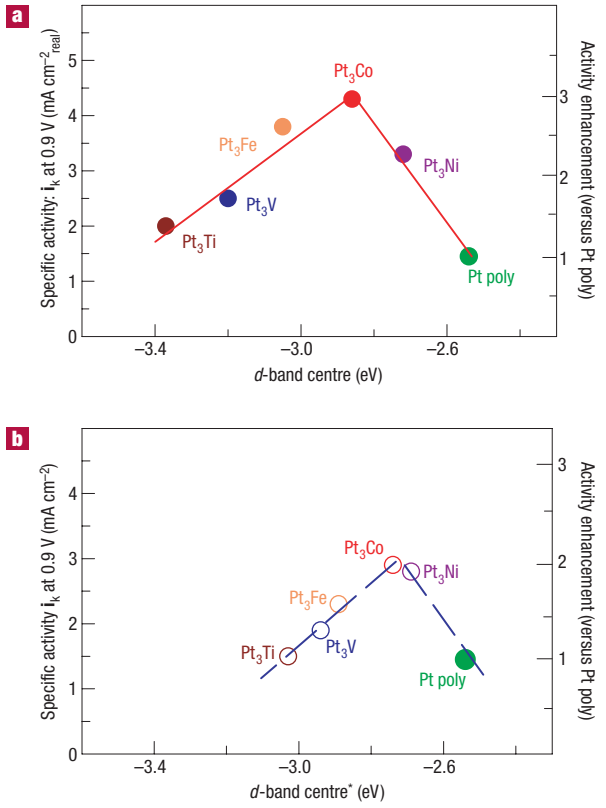

Figure 4 Relationships between the catalytic properties and electronic structure of Pt_3M alloys. a,**b**, Relationships between experimentally measured specific activity for the ORR on Pt_3M surfaces in 0.1 M $HClO_4$ at 333 K versus the *d*-band centre position for the Pt-skin (**a**) and Pt-skeleton (**b**) surfaces. **b** shows the *d*-band centre values* established in UHV, which may deviate in the electrochemical environment due to dissolution of non-Pt atoms.

of reactive intermediates. In deriving equation (1), it is assumed that the ORR takes place on electrodes that are modified by OH_{ad}, anions and the other non-reactive molecular species. The kinetic of O_2 reduction is determined by the number of free Pt sites available for the adsorption of O_2 (the $1-\Theta_{ad}$ term in equation (1)) and by the Gibbs energy of adsorption of O_2 and reactive intermediates (the ΔG_{ad} term in equation (1)) on metal surfaces pre-covered by OH_{ad}. This reaction pathway and rate expression is now used to establish: (1) the effects of the electronic properties on the kinetics of the ORR on Pt_3Fe surfaces and (2) electrocatalytic trends for Pt_3M catalysts.

A characteristic set of polarization curves (**i** versus **E**) for the ORR on Pt, Pt-skeleton and Pt-skin surfaces in 0.1 M $HClO_4$ at 333 K is summarized in Fig. 3b. For all three surfaces, the polarization curves exhibit two distinguishable potential regions. Starting at 0.05 V and scanning the electrode potential positively, well-defined diffusion limiting currents ($\mathbf{i}_D$) (0.2–0.7 V) are followed by a mixed kinetic-diffusion control region between $0.8\,V < E < 1.0\,V$. Further inspection of Fig. 3b reveals that, in accordance with the adsorption processes discussed above, the activity of the ORR increases in the order Pt < Pt-skeleton < Pt-skin. As the kinetic parameters for all surfaces, for example, the number of exchanged electrons (the $4e^-$ reduction; no peroxide production in Fig. 3b), the Tafel slope (the slope of a curve of overpotential or electrolytic polarization in volts versus the logarithm of current density) and the activation energies (20–25 kJ mol^{-1}) are almost identical, the reaction mechanism, a 'series $4e^-$ reduction', is the same. The fact that the average energy of the *d* states is different and downshifted on Pt electronically modified by subsurface Fe means that the fractional coverage by OH_{ad} is reduced on these surfaces compared with pure Pt, which is in agreement with recent theoretical studies for Pt–Co (ref. 31) and other Pt–M systems[20,32]. On that basis, the $\Theta_{OH_{ad}}$–**E** dependence is controlled by the *d*-band centre position and it is obvious that the energy of the metal *d* band is the key parameter that determines the kinetics of the ORR. This may explain both the enhanced catalytic activity on Pt_3Fe as well as the important finding that, under the same experimental conditions, the Pt-skin and Pt-skeleton electrodes are more stable than bulk Pt. The stability of Pt surface atoms during the ORR has been examined by *in situ* surface X-ray scattering studies of Pt_3M single-crystal surfaces and these results will be discussed elsewhere.

In a recent report[32], the electrocatalytic activity of the ORR on a thin film of Pt deposited onto single-crystal metal substrates was established as a function of either the calculated

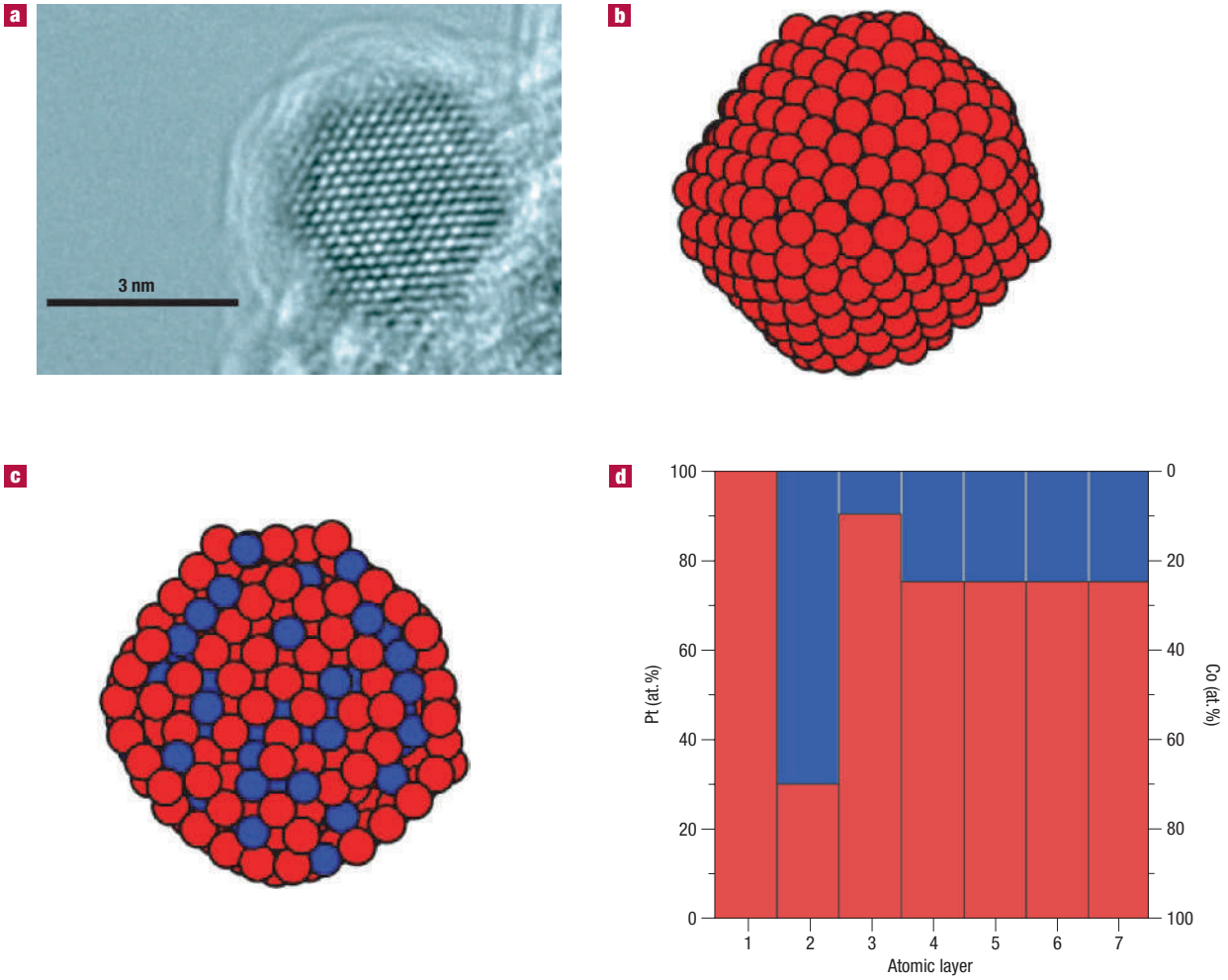

Figure 5 Nanoparticle catalysts. a, High-resolution transmission electron micrograph of a Pt_3Co nanoparticle. **b**,**c**, External (**b**) and cross-section (**c**) snapshots of a model Pt_3Co nanoparticle. **d**, Concentration profile for the Pt_3Co nanoparticle obtained from calculations.

binding energy of atomic oxygen or the calculated *d*-band centre. Although these results provided valuable information, it was not possible to establish real systematic experimental trends. By generalizing from the Pt_3Fe surfaces, described above, to the other Pt_3M surfaces, we now consider how the *d*-band centre position controls both the $(1-\Theta_{ad})$ term as well as the ΔG_{ad} term. To help visualize the general trends, the kinetic current at a constant overpotential is plotted as a function of the experimentally determined *d*-band centre position for the Pt-skin (and Pt-skeleton) surfaces. At this point, it is important to emphasize that the relationships summarized in Fig. 4 are unique in establishing a correlation between the experimentally determined surface electronic properties and reactivity when the average energy of the *d* states on the surface atoms is systematically changed across the periodic table. In particular, the relationship between the specific activity and the *d*-band centre position on the Pt-skin surfaces exhibits a volcano shape, with the maximum catalytic activity obtained for Pt_3Co. From Fig. 4b, it is obvious that the same trend applies for the Pt-skeleton surfaces, although the measured *d*-band centre of the Pt-skeleton surfaces in the electrochemical environment may deviate from the values obtained in UHV owing to dissolution of the 3*d* elements which also makes the surface morphology different to that on Pt-skin surfaces.

The overall consequence of this trend is that, to create better catalysts than Pt for the ORR, the catalysts should counterbalance two opposing effects, that is, a relatively strong adsorption energy of O_2 and reaction intermediates (O_2^-, O_2^{2-}, H_2O_2 and so on) and a relatively low coverage by spectator oxygenated species and specifically adsorbed anions. Therefore, for metal surfaces that bind oxygen/oxides/anions too strongly, for example, as in the case of Pt, the *d*-band centre is too close to the Fermi level and the rate of the ORR is limited by the availability of OH_{ad}/anion-free Pt sites. On the other hand, when the *d*-band centre is too far from the Fermi level, as in the case of Pt_3V and Pt_3Ti, the surface is less covered by OH_{ad} and anions, but the adsorption energy of O_2 and the intermediates is too low to enable a high turnover rate of the ORR. The resulting volcano, therefore, can be rationalized by the application of the Sabatier principle: that is, whereas for catalysts that bind oxygen too strongly, the rate is limited by the rate of removing surface oxides and anions, for catalysts that bind oxygen too weakly, the rate is limited by the rate of electron and proton transfer to adsorbed O_2.

The knowledge established by studying electrocatalytic trends on extended surfaces can be used to explain the activity pattern of the ORR on Pt_3M nanocatalysts[8,9,11] as well as to provide a fundamental basis for the improvement of existing cathode

nanocatalysts. Further affirmation of our approach has been accomplished from studies of the ORR on $Pt_3Ni(hkl)$ surfaces[33]. In the other set of experiments related to durability studies of fuel-cell catalysts, Pt_3Co nanoparticles showed improved stability and yielded an activity improvement of a factor of 2 compared with Pt nanoparticles of the same size[34]. It is important to emphasize that the ORR on the Pt_3Co-skeleton surface is also enhanced by a factor of 2 relative to bulk Pt (Fig. 4b) and that a clearly discernible difference in activity between extended Pt_3Co and Pt_3Ni alloys was also obtained for nanoparticles of the same composition[35]. It is, therefore, reasonable to propose that the near-surface composition and change in electronic properties of the Pt-skeleton alloys and the corresponding Pt_3M nanoparticles are essentially the same. The fact that electrocatalytic activity trends established for well-characterized bulk surfaces may also exist for nanoparticles is particularly important for engineering advanced catalysts with desired activity and/or selectivity. In particular, considering that the Pt_3Co-skin surface is the most active for the ORR (an activity improvement of a factor of 3 compared with Pt, see Fig. 4a), the challenge would be to create/tune PtCo nanoparticles with the electronic properties and segregation profile that correspond to the Pt-skin surface.

To explore this possibility, we carried out Monte Carlo (MC) simulations to predict whether the equilibrium cubo-octahedral $Pt_{75}Co_{25}$ nanoparticles, consisting of (111) and (100) facets bounded by low-coordination-number (edges and corners) atoms (see the high-resolution transmission electron micrograph in Fig. 5a), can have a nearly pure Pt monolayer shell and Co-enriched sublayer. The MC operations contain (1) atomic motions and (2) exchanges of two atoms with different element types. Thus, the $Pt_{75}Co_{25}$ nanoparticle, with a given initial configuration, undergoes both positional and compositional relaxation in the simulations. From the MC simulations at $T = 600$ K, it was found that the $Pt_{75}Co_{25}$ nanoparticle is thermodynamically stable even after 40×10^6 MC steps. Moreover, the equilibrium octahedral $Pt_{75}Co_{25}$ nanoparticle has a pure Pt monolayer shell and a Co-enriched sublayer, as shown in Fig. 5b–d from exterior and cross-section views that expose the outermost surface and centres of equilibrated nanoparticles containing 586 atoms (corresponding particle size of about 2.5 nm). The MC simulations reveal that, as in the case of the extended surfaces discussed above, it is possible to create a thermodynamically stable Pt skin on nanoscale surfaces. Catalytic enhancement by a factor of 3 would have a significant impact on fuel-cell technology. The total loading of Pt could be considerably reduced in fuel-cell stacks from 2.5 to 0.8 gPt kW^{-1}, which could lead to the earlier commercialization of polymer electrolyte membrane fuel cells.

Therefore, one way to increase the catalytic activity and stability of the Pt_3M nanoparticles for the ORR and, thus, to decrease the Pt loadings in the polymer electrolyte membrane fuel cell would be to create nanoclusters with electronic and morphological properties that mimic the extended Pt-skin surfaces. With the currently available techniques for nanoscale materials synthesis and characterization, it is feasible to tune the electronic properties of bi(multi)metallic nanoparticles in the same way as for the Pt_3M extended surfaces described in this work, resulting in a new generation of bi(multi)metallic systems with engineered nanoscale surfaces.

METHODS

EXPERIMENTAL

The AES and LEIS were carried out in a UHV system with a base pressure of 1×10^{-10} torr (ref. 18). AES spectra were recorded using the 3 keV electron beam energy and 3 eV_{p-p} modulation and a −5A beam current. LEIS were taken with a Ne^+ beam energy of 1 keV with a sample current from 5 to 30 nA at a residual Ne pressure of 2.5×10^{-8} torr. The UPS results were obtained at the Advanced Light Source synchrotron (ALS, LBNL) in a separate UHV system equipped with a hemispherical electron energy analyser. For the high-resolution valence-band photoemission spectra, the total energy resolution was less than 0.05 eV. The photon excitation energy was 90 eV. All spectra were measured at normal emission direction and the acceptance angle of the electron analyser was 5°. On each UPS measurement, the Shirley background was subtracted from the measured spectra. For the accurate comparison of all valence-band spectra, the upper level of integration of background subtraction was fixed at the 10.0 eV bonding energy position throughout all valence-band spectra. The p centre of the d-band calculation is defined as $\mu_p = \int N(\varepsilon)\varepsilon^p d\varepsilon$, where $N(\varepsilon)$ is the DOS and p is the order of moment. For example, μ_1/μ_0 is the first moment of DOS, or its centre of gravity. The UHV prepared/characterized Pt_3M electrodes were transferred from UHV into a rotating ring-disc electrode and, subsequently, immersed in electrolyte under potential control. Argon, oxygen and hydrogen gasses (Air Products, 5N8 purity) were bubbled through a glass frit into the electrolyte. The geometrical surface area of the disc electrode (well-characterized surface in UHV) was 0.283 cm^2 and all potentiodynamic surface exposures were done with a sweep rate of 50 mV s^{-1}. The active surface area in each case was established from cyclic voltammograms recorded in argon-purged electrolyte by integrating the charge in the hydrogen adsorption/desorption region, that is, from 0.0 to 0.4 V. Catalytic activities for ORR were established at 333 K in the potential range from 0 to 1.25 V. The values listed as specific activities for each alloy were obtained from several independent measurements in a rotating ring disc electrode. The activity enhancement factors and values listed as specific activities in Fig. 4 were revealed from several series of independent measurements. Cyclic voltammograms of Pt-skin and Pt-skeleton surfaces remained unchanged during and after ORR experiments, indicating that during the duration of the experiment (up to 4 h) both surfaces are rather stable. All potentials are referenced to the reversible hydrogen electrode (RHE) potential at the same temperature.

Received 14 December 2005; accepted 20 December 2006; published 18 February 2007.

References

1. Hoogers, G. & Thomsett, D. The role of catalysis in proton exchange membrane fuel cell technology. *Cat. Tech.* **3**, 106 (1999).
2. Markovic, N. M. & Ross, P. N. Jr. New electrocatalysts for fuel cells: from model surfaces to commercial catalysts. *Cat. Tech.* **4**, 110–126 (2000).
3. Dresselhause, M. S. & Thomas, I. L. Alternative energy technologies. *Nature* **414**, 332–337 (2001).
4. Schlapbach, L. & Züttel, A. Hydrogen-storage materials for mobile aplications. *Nature* **414**, 353–358 (2001).
5. Steele, B. C. H. & Heinzel, A. Materials for fuel-cell technologies. *Nature* **414**, 354–352 (2001).
6. Markovic, N. M. & Ross, P. N. Surface science studies of model fuel cell electrocatalysts. *Surf. Sci. Rep.* **45**, 117–230 (2002).
7. Vielstich, W., Lamm, A & Gasteiger, H. A. *Handbook of Fuel Cells, Fundamentals Technology and Applications* (Wiley, West Sussex, 2003).
8. Appleby, A. J. Electrocatalysis and fuel cells. *Catal. Rev.* **4**, 221–244 (1970).
9. Kinoshita, K. *Electrochemical Oxygen Technology* (Wiley, New York, 1992).
10. Toda, T., Igarashi, H., Uchida, H. & Watanabe, M. Enhancement of the electroreduction of oxygen on Pt alloys with Fe, Ni and Co. *J. Electrochem. Soc.* **146**, 3750–3756 (1999).
11. Markovic, N. M., Radmilovic, V. & Ross, P. N. in *Catalysis and Electrocatalysis at Nanoparticle Surfaces* (eds Wieckowski, A., Savinova, E. & Vayenas, C.) Ch. 9 (Marcel Dekker, New York, Basel, 2003).
12. Mukerjee, S. & Srinivasan, S. Enhanced electrocatalysis of oxygen reduction reaction on platinum alloys in proton-exchange membrane fuel-cells. *J. Electroanal. Chem.* **357**, 201–224 (1993).
13. Markovic, N. M., Gasteiger, H. A. & Ross, P. N. Kinetics of oxygen reduction reaction on Pt(9hkl) electrodes: Implication for the crystallite size effect with supported Pt electrocatalysts. *J. Electrochem. Soc.* **144**, 1591–1597 (1997).
14. Stamenkovic, V., Schmidt, T. J., Markovic, N. M. & Ross, P. N. Jr. Surface composition effects in electrocatalysis: kinetics of oxygen reaction on well defined Pt_3Ni and Pt_3Co alloy surfaces. *J. Phys. Chem. B* **106**, 11970–11979 (2002).
15. Stamenkovic, V., Schmidt, T. J., Ross, P. N. & Markovic, N. M. Surface segregation effects in electrocatalysis: kinetics of oxygen reduction reaction on polycrystalline Pt_3Ni alloy surfaces. *J. Electroanal. Chem.* **554**, 191–199 (2003).
16. Gauthier, Y., Baudoing-Savois, R., Bugnard, J. M., Bardi, U. & Atrei, A. Influence of the transition metal and order on the composition profile of $Pt_{80}M_{20}$ (111) (M = Ni, Co, Fe) alloy surfaces: LEED study of $Pt_{80}Co_{20}$ (111). *Surf. Sci.* **276**, 1–11 (1992).
17. Gauthier, Y. Pt-metal alloy surfaces: systematic trends. *Surf. Rev. Lett.* **3**, 1663–1689 (2001).
18. Mun, B. S., Lee, C., Stamenkovic, V., Markovic, N. M. & Ross, P. N. Electronic structure of Pd thin films on Re(0001) studied by high-resolution core-level and valence-band photoemission. *Phys. Rev. B* **71**, 115420–115426 (2005).
19. Norskov, J. K., Kitchin, J. R., Bligaard, J. R. & Joussen, T. Origin of the overpotential for oxygen reduction at a fuel cell cathode. *J. Phys. Chem. B* **108**, 17886 (2004).
20. Stamenkovic, V. *et al.* Changing the activity of electrocatalysts for oxygen reduction by tuning the surface electronic structure. *Angew. Chem. Int. Edn* **45**, 2897–2901 (2006).
21. Hammer, B. & Norskov, J. K. in *Chemisorption and Reactivity on Supported Clusters and Thin Films* (eds Lambert, R. M. & Pacchioni, G.) 285–351 (Kluwer Academic, 1997).

22. Greeley, J., Norskov, J. K. & Mavrikakis, M. Electronic structure and catalysis on metal surfaces. *Annu. Rev. Phys. Chem.* **53**, 319–348 (2002).
23. Xu, Y., Ruban, V. & Mavrikakis, M. Adsorption and dissociation of O_2 on PtCo and Pt–Fe alloys. *J. Am. Chem. Soc.* **126**, 4717–4725 (2004).
24. Greeley, J. & Mavrikakis, M. Alloy catalysts designed from first principles. *Nature Mater.* **3**, 810–815 (2004).
25. Markovic, N. M., Gasteiger, H. A. & Ross, P. N. Oxygen reduction on platinum low-index single-crystal surfaces in sulphuric acid solution: rotating ring-Pt(hkl) disk studies. *J. Phys. Chem.* **99**, 3411–3415 (1995).
26. Grgur, B. N., Markovic, N. M. & Ross, P. N. Jr. Temperature-dependent oxygen electrochemistry on platinum low-index single-crystal surfaces in acid solutions. *Can. J. Chem.* **75**, 1465–1471 (1997).
27. Markovic, N. M., Gasteiger, H. A., Grgur, B. N. & Ross, P. N. Oxygen reduction reaction on Pt(111): effects of bromide. *J. Electroanal. Chem.* **467**, 157–163 (1999).
28. Stamenkovic, V., Markovic, N. M. & Ross, P. N. Jr. Structure-relationships in electrocatalysis: oxygen reduction and hydrogen oxidation reaction on Pt(111) and Pt(100) in solution containing chloride ions. *J. Electroanal. Chem.* **500**, 44–51 (2000).
29. Tarasevich, M. R., Sadkowski, A. & Yeager, E. in *Comprehensive Treatise in Electrochemistry* (eds Bockris, J. O. M., Conway, B. E., Yeager, E., Khan, S. U. M. & White, R. E.) 301–398 (Plenum, New York, 1983).
30. Uribe, F., Wilson, M. S., Springer, T. & Gottesfeld, S. in *Proceedings of the Workshop on Structural Effects in Electrocatalytsis and Oxygen Electrochemistry* 92-11 (eds Scherson, D., Tryk, D., Daroux, M. & Xing, X.) 494–509 (The Electrochemical Society, Pennington, NJ, 1992).
31. Roques, J. & Anderson, A. B. Cobalt concentration effect in $Pt_{(1-x)}Co_x$ on the reversible potential for forming OH_{ads} from H_2O_{ads} in acid solution. *Surf. Sci.* **581**, 105–117 (2005).
32. Zhang, J., Vukmirovic, M. B., Xu, Y., Mavrikakis, M. & Adzic, R. R. Controlling the catalytic activity of platinum monolayer electrocatalysts for oxygen reduction with different substrates. *Angew. Chem.* **117**, 2170–2173 (2005).
33. Stamenkovic, V. R. *et al.* Improved oxygen reduction activity on $Pt_3Ni(111)$ via increased surface active sites. *Science* Published online 11 January 2007 (doi: 10.1126/science.1125941).
34. Mathias, M. F. *et al.* Two fuel cell cars in every garage? *Electrochemical Society-Interface* **14**, 24–35 (2005).
35. Paulus, U. A. *et al.* Oxygen reduction on carbon-supported Pt-Ni and Pt-Co alloy catalysts. *J. Phys. Chem. B* **106**, 4181–4191 (2001).

Acknowledgements

V.R.S. and N.M.M. acknowledge the support from the contract (DE-AC02-06CH11357) between UChicago Argonne, LLC and the US Department of Energy. We thank J. K. Nørskov and co-workers at the Technical University of Denmark for our ongoing collaboration on the design of catalysts for fuel cell reactions. We acknowledge the support of General Motors and helpful discussions with H. A. Gasteiger and F. T. Wagner. C.A.L. acknowledges the support of the EPSRC (UK). V.R.S. thanks M. W. West for support in experimental design.
Correspondence and requests for materials should be addressed to V.R.S. or N.M.M.

Competing financial interests

The authors declare that they have no competing financial interests.